

Thermal Conductivity of BAs under Pressure

Songrui Hou¹, Bo Sun², Fei Tian^{3,4}, Qingan Cai⁵, Youming Xu⁶, Shanming Wang⁷, Wanyue Peng⁵, Xi Chen⁶, Zhifeng Ren⁴, Chen Li^{1,5,*}, Richard B. Wilson^{1,5,*}

1) Materials Science and Engineering, University of California, Riverside, California 92521, USA

2) Tsinghua Shenzhen International Graduate School, Tsinghua University, Shenzhen, Guangdong 518055, China

3) School of Materials Science and Engineering, Sun Yat-sen University, Guangzhou, Guangdong 510275, China

4) Department of Physics and Texas Center for Superconductivity, University of Houston, Houston, Texas 77204, USA

5) Department of Mechanical Engineering, University of California, Riverside, California 92521, USA

6) Department of Electrical and Computer Engineering, University of California, Riverside, California 92521, USA

7) Department of Physics, Southern University of Science and Technology, Shenzhen, Guangdong 518055, China

*Correspondence should be addressed to chenli@ucr.edu and rwilson@ucr.edu

Abstract

Boron arsenide (BAs) is an ultrahigh-thermal-conductivity material with special phonon-phonon scattering behaviors. At ambient pressure, the bunching of acoustic phonon branches in BAs is believed to result in a small phase space for three-phonon scattering. Density functional theory predicts that this acoustic phonon bunching effect is sensitive to pressure and leads to an unusual pressure dependence of thermal conductivity. To explore this physics, we measure the thermal conductivity of BAs from 0 to 25 GPa using time-domain

thermoreflectance in a diamond anvil cell. We characterized two BAs samples with ambient thermal conductivities of 350 and 480 W m⁻¹ K⁻¹. Our experiments show that the thermal conductivity of both samples depends weakly on pressure from 0 to 25 GPa. We attribute the weak pressure dependence of the thermal conductivity of BAs to the weak pressure dependence of total phonon-phonon scattering rates. Our experimental results are consistent with DFT predictions that three-phonon scattering rates increase from 0 to 25 GPa, while four-phonon scattering rates decrease.

Introduction

High-thermal-conductivity materials are desirable for thermal management applications. Power electronic devices operate at power densities higher than 100 W/cm², roughly three orders of magnitude larger than the irradiance of the Sun^{1,2}. Discovery and integration of high thermal conductivity materials into electronics offer a route for increasing performance. However, discovery of such materials requires a detailed understanding of what properties lead to high thermal conductivity.

In the 1970s, Slack came up with four rules for finding non-metallic crystals with high thermal conductivity. These rules are: 1) low average atomic mass, 2) strong interatomic bonding, 3) simple crystal structure, and 4) low anharmonicity³. In 2013, Lindsay *et al.* used density functional theory (DFT) predictions to study the effects of atypical phonon dispersion and expanded Slack's rules^{4,5}. Phonon dispersion can have significant effects on three-phonon scattering rates by selection rules⁶. A large frequency gap between acoustic and optic phonon branches (a-o gap) reduces the phase space for three-phonon scattering processes involving two acoustic phonons and one optic phonon (*aa* processes). A large a-o gap exists in materials made up of heavy and light atoms, *e.g.*, boron and arsenic. Additionally, bunching of acoustic phonon branches also increases the thermal conductivity of a material. Acoustic phonon bunching happens when longitudinal and transverse phonons have similar frequencies across a significant volume of the Brillouin zone. The similar frequencies cause weak three-phonon scattering between longitudinal and transverse acoustic modes (*aaa* processes). A small phonon scattering phase space leads to a high thermal conductivity.

In BAs, the effect of an atypical phonon dispersion on thermal conductivity, Λ , is enormous. Simple models based on Slack's rules predict BAs has a $\sim 200 \text{ W m}^{-1} \text{ K}^{-1}$ thermal conductivity³. However, for high quality samples, experimentalists report room-temperature thermal conductivities of $\sim 1000 \text{ W m}^{-1} \text{ K}^{-1}$ ⁷⁻⁹. Such high thermal conductivity values are consistent with DFT predictions⁷⁻¹⁰.

Another way that BAs is an unusual thermal conductor is the importance of four-phonon scattering processes. In most crystals, four-phonon scattering events do not have an observable effect on thermal transport^{10,11}. However, DFT predictions suggest that three- and four-phonon scattering rates are comparable in BAs¹⁰. The temperature dependence of BAs's thermal conductivity also suggests four-phonon scattering processes are important⁷⁻⁹. When a material's thermal conductivity is limited by three-phonon scattering rates, the thermal conductivity is proportional to $1/T$ in the high temperature limit¹². However, between ~ 150 and 600 K , Λ of BAs shows a temperature dependence stronger than $1/T$, in agreement with DFT calculations that include effects of four-phonon scattering⁷⁻⁹.

The pressure dependence of BAs thermal conductivity offers the opportunity to experimentally explore the relationship between acoustic bunching, three- and four-phonon scattering, and thermal transport. DFT calculations predict that frequencies of longitudinal and transverse acoustic phonon branches separate with increasing pressure. In other words, pressurization on BAs reduces acoustic bunching (Fig. 1) and makes BAs's vibrational properties more like a typical crystal, *e.g.*, Si. As a result, DFT predicts three-phonon scattering rates increase with pressure, which leads to a rapidly decreasing thermal conductivity¹³⁻¹⁵. On the other hand, DFT calculations predict that four-phonon scattering rates decrease upon pressurization¹⁴. With both 3-phonon and 4-phonon scattering rates accounted, DFT predicts total phonon-phonon scattering rates depend weakly on pressure for $P < 20 \text{ GPa}$ ¹⁴. Then, as pressure increases above 20 GPa , DFT predicts the thermal conductivity gradually decreases¹⁴.

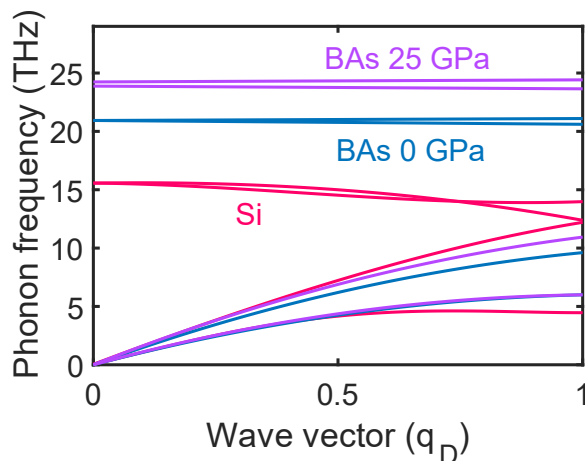


Fig. 1. Approximate phonon dispersion relations of BAs at 0 and 25 GPa. q_D is the Debye wave vector. Stiffening of the longitudinal acoustic phonon branch with increasing pressure reduces acoustic bunching. The dispersion relations of Si from Γ to X at 0 GPa are included as red curves¹⁶. Pressurization makes acoustic modes of BAs more like Si.

The aim of our experimental study is to use pressure to investigate phonon scattering mechanisms in BAs. We perform time-domain thermoreflectance (TDTR) measurements of BAs in a diamond anvil cell (DAC). TDTR is a well-established tool for measuring thermal conductivity¹⁷. Diamond anvil cells can generate pressures on the scale of GPa. We report the thermal conductivity as a function of pressure for two BAs samples with ambient thermal conductivities of 350 ± 40 and 480 ± 40 W m⁻¹ K⁻¹. We also measure the thermal conductivity of an MgO single crystal as a control experiment. The thermal conductivity of both BAs samples depends weakly on pressure between 0 and 25 GPa. Alternatively, for MgO, we observe a monotonically increasing thermal conductivity with increasing pressure.

A pressure independent thermal conductivity between 0 and 25 GPa is atypical behavior for nonmetallic materials. Simple models for phonon thermal conductivity predict a monotonic increase in thermal conductivity with increasing pressure³. At high pressures, usually, atomic bonds stiffen and phonon frequencies increase. Both effects favor a higher thermal conductivity. Furthermore, three-phonon scattering rates are governed by phonon anharmonicity. Anharmonicity typically decreases with increasing pressure. This is evidenced by the fact that most material's Grüneisen parameter decrease upon

compression¹⁸. Therefore, in most nonmetallic materials, three-phonon scattering rates are expected to decrease with increasing pressure, which favors a larger thermal conductivity at a higher pressure.

To better understand the atypical pressure dependence of BAs's Λ , we use a relaxation time approximation (RTA) model to analyze our experimental results. The RTA model examines how pressure induced changes in phonon group velocities, phonon-phonon scattering, and defect scattering affect Λ vs. P . Our RTA analysis suggests the weak pressure dependence of Λ on P is because total phonon-phonon scattering rates are pressure independent. Therefore, we conclude that our experiments are consistent with DFT predictions for how acoustic bunching, three-phonon scattering, and four-phonon scattering govern Λ vs. P in BAs¹⁴.

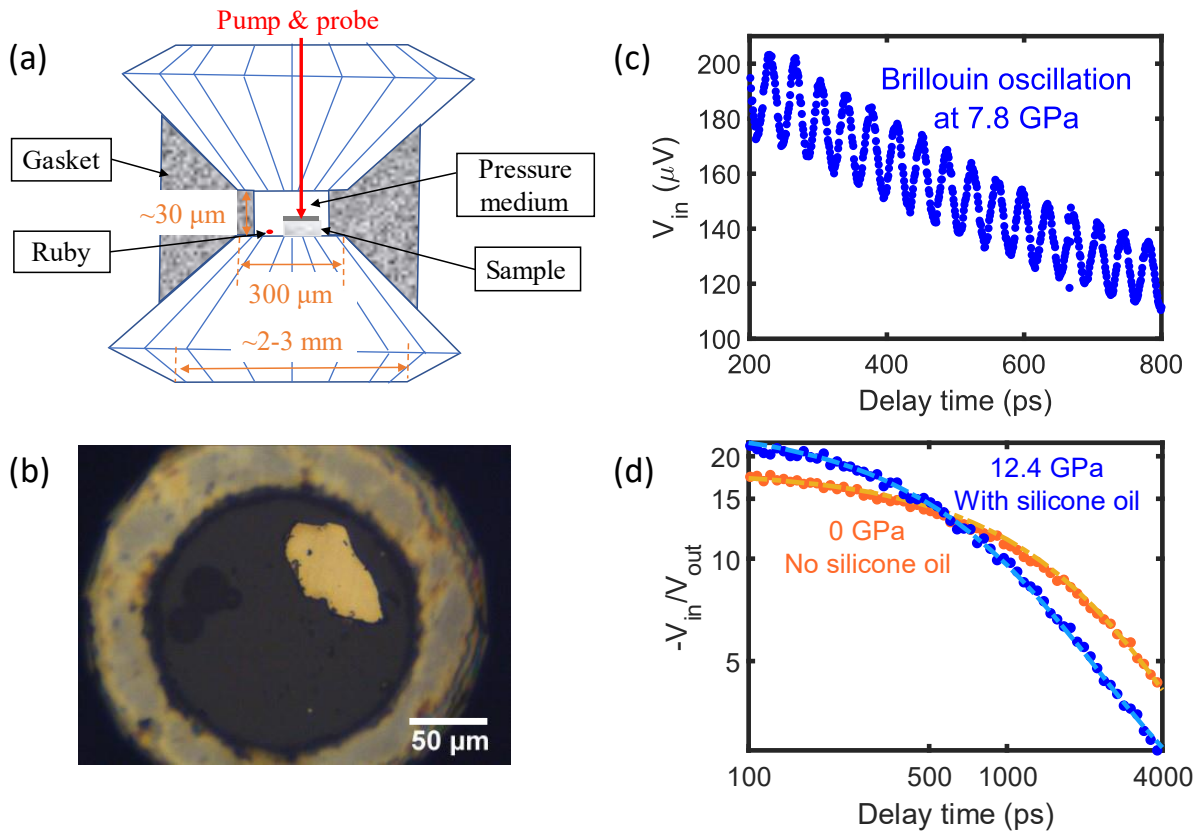


Fig. 2. (a) A schematic of the DAC assisted TDTR measurement. The pump and probe beams transmit through the diamond and silicone oil, and are focused onto the sample surface. (b) Image of a BAs sample (Sample B) coated with Al inside a DAC. We also load ruby spheres. The fluorescence spectrum of ruby allows measurement of the pressure in the DAC. We use a stainless-steel gasket and silicone-oil pressure medium. (c) An example of Brillouin oscillations from the silicone oil in our experimental signal. The frequency of the Brillouin oscillation provides a sensitive measure of local pressure at the sample. (d) TDTR data of sample A at 0 and 12.4 GPa. The dots and lines are the experimental results and the predictions by the heat diffusion model, respectively.

Results

In Fig. 3, we show the thermal conductivity vs. pressure of the two BAs samples. As described in Methods, we performed multiple TDTR measurements at various locations on the BAs samples at each pressure. The thermal conductivity reported in Fig. 3 is the average value from all measurements for a given sample and pressure. The error bars in Fig. 3 denote the standard deviation in thermal conductivity observed between measurements. We show the thermal conductivity vs. pressure for each measured spot in Supplementary Fig. S6 and S7.

For both samples, we observe that the thermal conductivity has a weak pressure dependence. At nearly all pressures, we observe a thermal conductivity variation within 10% of the value we observe at 0 GPa. We show raw data and thermal model fits at a variety of pressures in Supplementary Fig. S9.

In both samples, we observed Λ values that deviate from the overall trend between 4 and 6 GPa. We are not certain what the origin of this off-trend behavior is. However, the off-trend behavior may be related to the significant changes in Al's optical properties at 1.58 eV across this pressure range. The optical properties of Al near 1.5 eV are strongly affected by absorption due to interband transitions¹⁹. Upon pressurization, the interband transition energy threshold increases, which causes the thermoreflectance at 1.58 eV crossing through zero and changing sign²⁰. We observe significant changes in the amplitude of thermoreflectance and picosecond acoustic signals in our data in this pressure range. We also observe the Al thermoreflectance flips its sign at ~6 GPa.

The standard deviation in Λ we observe across multiple locations is ~10-15% at most pressures. At some pressures, standard deviation is larger, *e.g.*, >20%. We are not certain about why variance increased in these measurements, but believe it is related to the quality of the sample surface. Variance with laser position on the sample is smaller in Sample B than Sample A [see Supplementary Fig. S6 and S7]. For Sample B, we coated the sample with Al after polishing to reduce thickness. This modification in sample preparation procedure improved surface quality. Another possibility is all measurements on Sample B are localized to

a smaller region than on Sample A (see Supplementary Fig. S1). We note that, regardless of whether the pressures with large error bars are included or excluded from the data set for Λ vs. P , overall trends are unaffected.

The weak pressure dependence we observe in BAs is in stark contrast with our observations for MgO, see Fig. 4. For MgO, we observe an increase in the thermal conductivity by $\sim 2\times$ upon compression to 20 GPa. Our results on MgO agree with prior reports²¹.

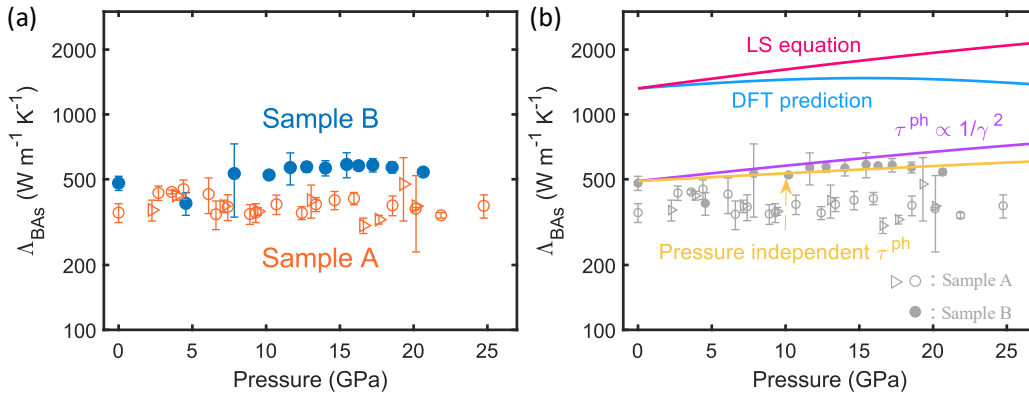


Fig. 3. (a) Pressure dependent thermal conductivities of BAs Sample A and B. Open and filled circles are compression data while triangles are decompression data. (b) Model predictions for the thermal conductivity of BAs. The blue curve is the DFT prediction from Ref. 14. The red line represents the Leibfried-Schlömann equation prediction. The purple and yellow lines are relaxation time approximation model predictions. The RTA model considers the effect of phonon-phonon scattering and phonon-defect scattering. We assume the pressure dependence of the phonon-phonon scattering rate is governed by a scattering amplitude, A . For the purple line, we assume $A \propto \gamma^2$ under pressures where γ is the Grüneisen parameter. For the yellow line, we assume a pressure independent A .

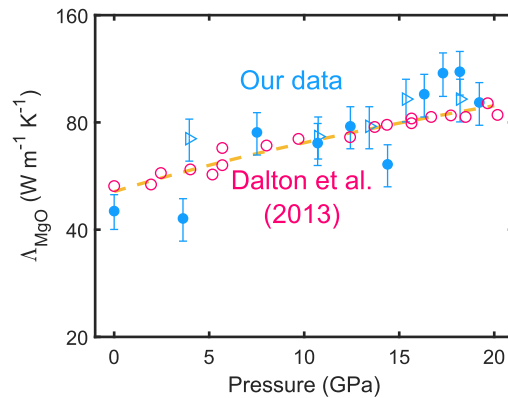


Fig. 4. Pressure dependent thermal conductivities of MgO. Blue dots and triangles are data collected during compression and decompression, respectively. For MgO, we measured only a single location at each pressure. The error bars here represent the $\sim 10\%$ uncertainty in thermal conductivity that arises from uncertainty in thermal model parameters. Red circles and the orange dashed line are the experimental data and prediction of the Leibfried-Schlömann equation, both from Ref. 21.

Discussion and Analysis

In the absence of contextualizing information, the dramatic difference in $\Lambda(P)$ for BAs vs. MgO (Fig. 3 vs. Fig. 4) is quite surprising. The bulk modulus of BAs is 142 GPa, while MgO is 160 GPa^{22,23}. Both materials have a relatively small atomic mass per unit cell and simple unit cells. The Grüneisen parameter of BAs and MgO are both expected to experience a ~13% decrease between 0 and 20 GPa^{24,25}.

The strong pressure dependence of MgO's thermal conductivity is typical, and the weak pressure dependence of BAs's thermal conductivity is not. We base this conclusion by surveying experimental results for Λ vs. P of other nonmetallic materials across a similar pressure range. MgSiO₃'s thermal conductivity increases from 6 to 10 W m⁻¹ K⁻¹ upon compression to 20 GPa²⁶. The thermal conductivity of various ferropericlasite materials roughly doubles upon compression to 20 GPa²⁶. Ice VII's thermal conductivity increases from 4 to 25 W m⁻¹ K⁻¹ between 2 and 22 GPa²⁷. PMMA's thermal conductivity increases by a factor of 3 upon pressurization from 0 to ~10 GPa²⁸. The thermal conductivity of muscovite mica, KAl₂(Si₃Al)O₁₀(OH)₂, increases by a factor of 10 between 0 and 20 GPa²⁹. In a recent review article, Hofmeister reports the $d\Lambda/dP$ for 22 materials³⁰. 21 out of 22 materials have positive derivatives that are larger than 3.5% per GPa. Materials whose thermal conductivity do not monotonically increase with pressure often involve a phase transition, *e.g.* Si³¹ or KCl³². BAs is not expected to undergo a phase transition below 100 GPa³³.

The thermal conductivity of a material is determined by group velocities, number density, and relaxation times of phonons. Therefore, Λ vs. P is determined by the pressure dependence of these three vibrational properties. The Leibfried-Schlömann (LS) equation is a simple model for quantifying how these three vibrational properties govern Λ . A number of prior experimental studies show the LS equation often has predictive power in explaining Λ vs. P ^{21,27,29}. The LS equation predicts

$$\Lambda = \frac{B\bar{M}\delta\theta^3}{T\gamma^2}. \quad (1)$$

Here B is a constant, \bar{M} is the average mass of an atom in the crystal, δ^3 is the average volume occupied by one atom in the crystal, θ is the Debye temperature, T is temperature, and γ is the Grüneisen parameter. We take the pressure dependence of these quantities for BAs from Refs. 25,33. Not surprisingly given BAs' special phonon properties, the LS equation drastically overestimates the pressure dependence of Λ in BAs, see Fig. 3(b). Alternatively, it does a good job predicting Λ vs. P in MgO, see Fig. 4. One note here is that the calculated ambient Grüneisen parameter of BAs in Ref. 25 is larger than the experimental result³⁴. However, what we care about is the pressure dependence of the Grüneisen parameter instead of the ambient value.

In contrast to the LS equation, DFT predictions by Ravichandran and Broido¹⁴ nicely explains $d\Lambda/dP \approx 0$ at $P < 20$ GPa, as shown in Fig. 3(b). DFT predicts that increases in phonon group velocity and phonon number density are offset by decreases in the phonon-phonon scattering rates^{5,14,15}. We believe this is the most likely explanation for our data. However, there is an important difference between our BAs samples and the ideal material evaluated in Ref. 14. Our samples have defects^{35,36}. The thermal conductivity of Sample A and B are 50~70% lower than the ~ 1000 W m⁻¹ K⁻¹ values previously reported for high purity single crystals⁷⁻⁹. The most likely source of the lower thermal conductivity is phonon-defect scattering. Previous studies suggest there could be many kinds of defects in BAs^{35,37,38}. A boron or arsenic vacancy concentration of $\sim 1.5 \times 10^{19}$ cm⁻³ would be sufficient to explain the reduced Λ of our samples³⁷. As_B-B_{As} antisite pairs of $\sim 1.5 \times 10^{19}$ cm⁻³ concentration would explain $\Lambda \sim 500$ W m⁻¹ K⁻¹ of BAs³⁸. A recent research suggests $\sim 10^{20}$ cm⁻³ carbon impurity concentration also could result in the Λ reduction of our samples³⁵. Another contributor to the lower thermal conductivity is the laser spot sizes in our TDTR measurements are comparable to phonon mean-free-paths^{39,40}. We report the spot size dependent thermal conductivity of Sample B in the Supplementary Fig. S5, along with a comparison with previously reported data⁷. The ambient thermal conductivity of Sample B is ~ 620 W m⁻¹ K⁻¹ when using a ~ 13 - μ m-radius spot size in the TDTR measurement.

We believe that phonon-defect scattering does not explain the unusual Λ vs. P trend we observe in our BAs samples. Phonon-defect scattering rates may reduce the pressure-dependence of phonon relaxation times. However, a survey of the literature reveals $d\Lambda/dP$ remains large and positive, even in materials where phonon-defect scattering is the primarily limiter of phonon mean-free-paths²⁶. For example, alloying MgO with 8% Fe causes the ambient thermal conductivity to reduce from 53 W m⁻¹ K⁻¹ to 5 W m⁻¹ K⁻¹, but the $d\Lambda/dP$ change from ~4 % per GPa to 8 % per GPa²⁶.

For Λ be pressure independent, phonon relaxation times need to decrease with increasing pressure. To show this, we constructed a simple relaxation time approximation model to quantitatively evaluate how various vibrational properties govern Λ vs. P dependence. In our model, we consider the pressure dependence of (1) phonon group velocity, (2) phonon number density, (3) total rates of phonon-phonon scattering, and (4) phonon-defect scattering rates. We set the pressure dependence of phonon group velocities and density of states to mimic DFT predictions^{14,25,41}. We assume the total phonon-phonon scattering rate is $\tau_{pp}^{-1} = Af(\omega)$. Here, A is a pressure dependent scattering amplitude, and $f(\omega)$ is a function chosen to mimic the frequency dependence of τ_{pp}^{-1} predicted by DFT calculations accounting for both 3- and 4-phonon processes¹⁴. We set the magnitude of A at 0 GPa so that $\Lambda \approx 1300$ W m⁻¹ K⁻¹. Finally, to model phonon-defect scattering rates, we assume a frequency dependent point-defect scattering rate like the one described in Ref. 42. Further details of our RTA model are provided in Supplemental Materials.

In Fig. 3(b), we show the prediction of our RTA model with two different assumptions on how A depends on pressure. The purple curve assumes $A \propto \gamma^2(P)$. Alternatively, for the yellow curve, we assume A is independent of pressure. The pressure dependent γ is from DFT calculations²⁵. We find that the pressure independent A does a reasonable job reproducing our experimental observation of $d\Lambda/dP \approx 0$ for $P < 25$ GPa. In the DFT prediction, the relaxation times due to all phonon-phonon scattering processes change very little at pressures below 30 GPa¹⁴.

In conclusion, we measured the pressure dependent thermal conductivity of two BAs samples between 0 and 25 GPa. In contrast to the typical behavior for nonmetallic materials, we observe weak pressure dependence. We attribute the weak pressure dependence of Λ to pressure independent phonon-phonon scattering rates at $P < 25$ GPa. Our results are consistent with DFT models for how the pressure dependence of acoustic phonon bunching affects three- and four-phonon scattering rates. Our results improve fundamental understanding of the complex interplay between phonon dispersion, phonon scattering, and thermal transport in high thermal conductivity materials.

Methods

Materials synthesis

Single crystal BAs (space group: $F\bar{4}3m$) samples are grown by chemical vapor transport (CVT). The reactants are pure boron bulk particles (Alfa Aesar, 99.9999%) and arsenic lumps (Alfa Aesar, > 99.99999+%). We employ small amount of iodine powder (Alfa Aesar, 99.999%) as the transport agent. Details about the synthesis can be found in Ref. 43. We include X-ray diffraction and Raman scattering data on BAs in Supplementary Fig. S2.

Sample preparation

We prepared two pieces of BAs for DAC experiments. The first sample, which we label as Sample A, was first coated with a ~90-nm-thick Al film by electron beam evaporation. After coating, we polished the BAs from the uncoated side down to $\sim 7 \pm 2$ μm . The final thickness was measured with an optical microscope. We loaded one $\sim 50 \times 80$ μm sample into a DAC with a culet size of 300 μm . For the second sample, labelled Sample B, we changed our procedure to improve the surface quality. We first polished a piece of BAs crystal down to $\sim 7 \pm 2$ μm . Then, we deposited a ~ 90 -nm-thick Al film on the sample. We loaded ruby spheres alongside the samples as pressure indicators. We used silicone oil (Polydimethylsiloxane, CAS No. 63148-62-9 from ACROS ORGANICS) as the pressure medium for both measurements.

We used 250 μm thick stainless-steel gaskets and pre-indented them in our DAC to a thickness between 30 to 60 μm . Then we drilled holes with a diameter of ~ 170 μm at the center of the indentations by a laser drill system. The holes serve as containers for the samples, ruby spheres, and pressure medium.

Time-domain thermoreflectance (TDTR) in diamond anvil cells

We measured the thermal conductivity of BAs at ambient and high pressures by TDTR. TDTR is a well-established pump-probe technique. In TDTR measurements, a train of 785-nm-wavelength laser pulses emitted from a mode-locked Ti:sapphire oscillator is split into a pump beam and a probe beam. The pump beam heats the sample at a modulation frequency of 10.1 MHz. The probe beam monitors the temperature decay at the sample surface via temperature induced changes in reflectance. The reflected probe beam from the sample surface is collected by a silicon photodiode detector (Thorlabs DET10A2). A lock-in amplifier reads the micro-volt change in voltage output by the detector due to changes in reflected probe beam intensity. The amplifier outputs the in-phase signal V_{in} and out-of-phase signal V_{out} at the 10.1 MHz pump modulation frequency. TDTR measurements were performed at Tsinghua Shenzhen International Graduate School.

Fig. 2(a) shows a schematic of the TDTR measurement in a DAC. The pump and probe beams go through the diamond anvil and silicone oil, and reach the sample surface. Fig. 2(b) shows a photo of Sample B loaded inside a DAC. The pressure of the system is calibrated using the pressure dependent shift of the R1 line in the ruby fluorescence spectrum⁴⁴. We also use the Brillouin frequency of silicone oil as a second measure of pressure⁴⁵. Fig. 2(c) shows a Brillouin oscillation that we observe in our experimental TDTR signals. When the pump beam heats the Al surface, it launches a strain wave into the silicone oil medium. The strain wave front moves at the speed of sound of silicone oil. Both the strain wave and Al can reflect the subsequent probe beam. These two reflected probe beams interfere with each other and cause Brillouin oscillations in the V_{in} signal⁴⁶.

We used the beam-offset method to measure the laser spot size⁴⁷. The $1/e^2$ radius was 5.1 μm and 4.5 μm for the measurements on Sample A and B, respectively.

We observed ~10-15% variation in the TDTR derived thermal conductivity depending on the measured locations on the samples. We attribute these variations to two factors. First, sample defects or inhomogeneities can affect TDTR signals. We tried to avoid visible defects on the sample's surface, but processing of the sample for DAC measurements led to less than perfectly smooth and clean surfaces. A second reason for variation is likely intrinsic to the crystal. Prior studies of BAs crystals report a Λ variation of ~10-15% across the crystal surface⁷. To minimize the effect of this location sensitivity in our $\Lambda(P)$ measurements, we initially tried to restrict our experiments to a single location at all pressures. However, this proved challenging for several reasons. Changing the DAC pressure requires removing the DAC from the TDTR setup, and then resetting up our experiment. Furthermore, the sample undergoes a small amount of deformation upon pressurization. To cope with these challenges, we changed our approach. Instead of trying to restrict our experiment to a single location, we performed TDTR scans at multiple locations on the samples at each pressure. We measured four spots which were ~8 μm away from each other on Sample A. We measured five spots which were ~2 μm away from each other on Sample B (see Supplementary Fig. S1). The thermal conductivity values we report for Sample A and B are the average from all four or five spots, respectively.

As a control experiment, we measured the pressure dependent thermal conductivity of a MgO sample. The pressure dependence of MgO's thermal conductivity is well studied experimentally²¹ and theoretically^{14,48}. We prepared the MgO sample following similar procedures as Sample A (coat with Al first, then polish to reduce thickness). Then we performed TDTR measurements at pressures between 0 and 19 GPa. The $1/e^2$ beam radius for measurements of MgO was ~3 μm .

Data analysis of TDTR under pressure

We use a bidirectional heat diffusion model to analyze the collected TDTR data¹⁷. The bidirectional model accounts for heat flow from the Al transducer into both the BAs and silicone oil. The thermal conductivity, heat capacity and thickness of each layer are the input parameters in the heat diffusion model. Therefore, we must estimate how these parameters evolve with pressure to interpret our TDTR data. Below, we describe how we account for the pressure dependence of all parameters.

Prior to loading the sample into the DAC, we measure the Al film thickness by picosecond acoustics⁴⁶. At high pressures, we assume BAs shrinks equally in every direction since BAs is a cubic crystal³³. If the volume of BAs at pressure P is V_P , and the in-plane area is S_P , then $S_P = S_0 \cdot (V_P / V_0)^{\frac{2}{3}}$. Here, V_0 and S_0 are volume and area of BAs at 0 GPa. We assume the in-plane area of Al is equal to S_P . Then the thickness of Al at pressure P will be $h_P \approx V_P^{Al} / S_P$. Here, V_P^{Al} is the Al volume at pressure P based on Al's equation of state⁴⁹.

To estimate the pressure dependence of Al's heat capacity, we follow Ref. 45, and use a Debye model. For silicone oil, we use previously reported pressure dependent heat capacities and thermal conductivities⁵⁰.

To model the pressure-dependence of BAs's heat capacity, we use a simple isotropic model for the phonon dispersion. We assume $\omega = v_s k - A k^2$. Here ω is the phonon frequency, v_s is the longitudinal or transverse speed, k is the wavevector magnitude, and A is a constant. The value of A is determined by the phonon frequency at the Brillouin zone boundary. We set the values of v_s and A to mimic DFT predictions for phonon dispersion relations vs. pressure^{14,51}. Fig. 1 shows the constructed longitudinal and transverse phonon dispersion relations at 0 and 25 GPa. From the phonon dispersion, we calculate the heat capacities [see equation (1) in Supplementary Materials].

Finally, to interpret the pressure dependent TDTR measurements of MgO, we use the heat-capacity data reported in Ref. 21.

References

1. Qian, C. *et al.* Thermal Management on IGBT Power Electronic Devices and Modules. *IEEE Access* **6**, 12868–12884 (2018).
2. Willson, R. C. & Hudson, H. S. Solar luminosity variations in solar cycle 21. *Nature* **332**, 810–812 (1988).
3. Slack, G. A. Nonmetallic crystals with high thermal conductivity. *J. Phys. Chem. Solids* **34**, 321–335 (1973).
4. Lindsay, L., Broido, D. A. & Reinecke, T. L. First-Principles Determination of Ultrahigh Thermal Conductivity of Boron Arsenide: A Competitor for Diamond? *Phys. Rev. Lett.* **111**, 025901 (2013).
5. Broido, D. A., Lindsay, L. & Reinecke, T. L. Ab initio study of the unusual thermal transport properties of boron arsenide and related materials. *Phys. Rev. B - Condens. Matter Mater. Phys.* **88**, 1–12 (2013).
6. Lax, M., Hu, P. & Narayanamurti, V. Spontaneous phonon decay selection rule: N and U processes. *Phys. Rev. B* **23**, 3095–3097 (1981).
7. Sheng, L. *et al.* High thermal conductivity in cubic boron arsenide crystals. *Science* **361**, 579–581 (2018).
8. Fei, T. *et al.* Unusual high thermal conductivity in boron arsenide bulk crystals. *Science* **361**, 582–585 (2018).
9. Kang, J. S., Li, M., Wu, H., Nguyen, H. & Hu, Y. Experimental observation of high thermal conductivity in boron arsenide. *Science* **361**, 575–578 (2018).
10. Feng, T., Lindsay, L. & Ruan, X. Four-phonon scattering significantly reduces intrinsic thermal conductivity of solids. *Phys. Rev. B* **96**, 1–6 (2017).
11. Lindsay, L. & Broido, D. A. Three-phonon phase space and lattice thermal conductivity in semiconductors. *J. Phys. Condens. Matter* **20**, (2008).

12. Roufousse, M. C. & Klemens, P. G. Lattice Thermal Conductivity of Minerals at High Temperatures. *J. Geophys. Res.* **79**, (1974).
13. Lindsay, L., Broido, D. A., Carrete, J., Mingo, N. & Reinecke, T. L. Anomalous pressure dependence of thermal conductivities of large mass ratio compounds. *Phys. Rev. B - Condens. Matter Mater. Phys.* **91**, 1–5 (2015).
14. Ravichandran, N. K. & Broido, D. Non-monotonic pressure dependence of the thermal conductivity of boron arsenide. *Nat. Commun.* **10**, 1–8 (2019).
15. Wang, L. *et al.* High-pressure phases of boron arsenide with potential high thermal conductivity. *Phys. Rev. B* **99**, 174104 (2019).
16. Yin, M. T. & Cohen, M. L. Ab initio calculation of the phonon dispersion relation: Application to Si. *Phys. Rev. B* **25**, 4317–4320 (1982).
17. Cahill, D. G. Analysis of heat flow in layered structures for time-domain thermoreflectance. *Rev. Sci. Instrum.* **75**, 5119–5122 (2004).
18. Boehler, R. & Ramakrishnan, J. Experimental results on the pressure dependence of the Gruneisen parameter: A Review. *J. Geophys. Res. Solid Earth* **85**, 6996–7002 (1980).
19. Rosei, R. & Lynch, D. W. Thermomodulation Spectra of Al, Au, and Cu. *Phys. Rev. B* **5**, 3883–3894 (1972).
20. Hsieh, W.-P. & Cahill, D. G. Ta and Au(Pd) alloy metal film transducers for time-domain thermoreflectance at high pressures. *J. Appl. Phys.* **109**, 113520 (2011).
21. Dalton, D. A., Hsieh, W. P., Hohensee, G. T., Cahill, D. G. & Goncharov, A. F. Effect of mass disorder on the lattice thermal conductivity of MgO periclase under pressure. *Sci. Rep.* **3**, 1–5 (2013).
22. Tian, F. *et al.* Mechanical properties of boron arsenide single crystal. *Appl. Phys. Lett.* **114**, (2019).
23. Karki, B. B. *et al.* Structure and elasticity of MgO at high pressure. *Am. Mineral.* **82**, 51–60 (1997).
24. Karki, B. B., Wentzcovitch, R. M., de Gironcoli, S. & Baroni, S. High-pressure lattice dynamics and thermoelasticity of MgO. *Phys. Rev. B* **61**, 8793–8800 (2000).

25. Daoud, S., Bioud, N. & Lebga, N. Elastic and thermophysical properties of BAs under high pressure and temperature. *Chin. J. Phys.* **57**, 165–178 (2019).
26. Deschamps, F. & Hsieh, W. P. Lowermost mantle thermal conductivity constrained from experimental data and tomographic models. *Geophys. J. Int.* **219**, S115–S136 (2019).
27. Chen, B., Hsieh, W. P., Cahill, D. G., Trinkle, D. R. & Li, J. Thermal conductivity of compressed H₂O to 22 GPa: A test of the Leibfried-Schlömann equation. *Phys. Rev. B - Condens. Matter Mater. Phys.* **83**, 1–4 (2011).
28. Hsieh, W. P. *et al.* Testing the minimum thermal conductivity model for amorphous polymers using high pressure. *Phys. Rev. B - Condens. Matter Mater. Phys.* **83**, 1–5 (2011).
29. Hsieh, W. P., Chen, B., Li, J., Keblinski, P. & Cahill, D. G. Pressure tuning of the thermal conductivity of the layered muscovite crystal. *Phys. Rev. B - Condens. Matter Mater. Phys.* **80**, 1–4 (2009).
30. Hofmeister, A. M. Pressure dependence of thermal transport properties. *Proc. Natl. Acad. Sci.* **104**, 9192 LP – 9197 (2007).
31. Hohensee, G. T., Fellingner, M. R., Trinkle, D. R. & Cahill, D. G. Thermal transport across high-pressure semiconductor-metal transition in Si and Si_{0.991}Ge_{0.009}. *Phys. Rev. B - Condens. Matter Mater. Phys.* **91**, 1–12 (2015).
32. Andersson, P. Thermal conductivity under pressure and through phase transitions in solid alkali halides. I. Experimental results for KCl, KBr, KI, RbCl, RbBr and RbI. *J. Phys. C Solid State Phys.* **18**, 3943–3955 (1985).
33. Greene, R. G., Luo, H., Ruoff, A. L., Trail, S. S. & DiSalvo, F. J. Pressure induced metastable amorphization of BAs: Evidence for a kinetically frustrated phase transformation. *Phys. Rev. Lett.* **73**, 2476–2479 (1994).
34. Chen, X. *et al.* Thermal Expansion Coefficient and Lattice Anharmonicity of Cubic Boron Arsenide. *Phys. Rev. Appl.* **11**, 064070 (2019).

35. Chen, X. *et al.* Effects of Impurities on the Thermal and Electrical Transport Properties of Cubic Boron Arsenide. *Chem. Mater.* **33**, 6974–6982 (2021).
36. Meng, X. *et al.* Pressure-Dependent Behavior of Defect-Modulated Band Structure in Boron Arsenide. *Adv. Mater.* **32**, 2001942 (2020).
37. Protik, N. H., Carrete, J., Katcho, N. A., Mingo, N. & Broido, D. Ab initio study of the effect of vacancies on the thermal conductivity of boron arsenide. *Phys. Rev. B* **94**, 1–7 (2016).
38. Zheng, Q. *et al.* Antisite Pairs Suppress the Thermal Conductivity of BAs. *Phys. Rev. Lett.* **121**, 105901 (2018).
39. Wilson, R. B. & Cahill, D. G. Anisotropic failure of Fourier theory in time-domain thermoreflectance experiments. *Nat. Commun.* **5**, 5075 (2014).
40. Minnich, A. J. *et al.* Thermal Conductivity Spectroscopy Technique to Measure Phonon Mean Free Paths. *Phys. Rev. Lett.* **107**, 095901 (2011).
41. Hadjiev, V. G., Iliev, M. N., Lv, B., Ren, Z. F. & Chu, C. W. Anomalous vibrational properties of cubic boron arsenide. *Phys. Rev. B* **89**, (2014).
42. Tamura, S. Isotope scattering of dispersive phonons in Ge. *Phys. Rev. B* **27**, 858–866 (1983).
43. Tian, F. *et al.* Seeded growth of boron arsenide single crystals with high thermal conductivity. *Appl. Phys. Lett.* **112**, (2018).
44. Mao, H. K., Xu, J. & Bell, P. M. Calibration of the ruby pressure gauge to 800 kbar under quasi-hydrostatic conditions. *J. Geophys. Res.* **91**, 4673 (1986).
45. Hohensee, G. T., Wilson, R. B. & Cahill, D. G. Thermal conductance of metal-diamond interfaces at high pressure. *Nat. Commun.* **6**, 1–9 (2015).
46. Thomsen, C., Maris, H. J. & Tauc, J. Picosecond acoustics as a non-destructive tool for the characterization of very thin films. *Thin Solid Films* **154**, 217–223 (1987).
47. Feser, J. P. & Cahill, D. G. Probing anisotropic heat transport using time-domain thermoreflectance with offset laser spots. *Rev. Sci. Instrum.* **83**, (2012).

48. Tang, X. & Dong, J. Lattice thermal conductivity of MgO at conditions of Earth's interior. *Proc. Natl. Acad. Sci.* **107**, 4539 LP – 4543 (2010).
49. Greene, R. G., Luo, H. & Ruoff, A. L. Al as a Simple Solid: High Pressure Study to 22t| GPa (2. 2 Mbar). **73**, 11–14 (1994).
50. Hsieh, W. P. Thermal conductivity of methanol-ethanol mixture and silicone oil at high pressures. *J. Appl. Phys.* **117**, (2015).
51. Daoud, S., Bioud, N. & Bouarissa, N. Structural phase transition, elastic and thermal properties of boron arsenide: Pressure-induced effects. *Mater. Sci. Semicond. Process.* **31**, 124–130 (2015).

Acknowledgements

This research was supported as part of ULTRA, an Energy Frontier Research Center funded by the U.S. Department of Energy (DOE), Office of Science, Basic Energy Sciences (BES), under Award # DE-SC0021230 (thermal modelling), and by the National Science Foundation (NSF) under Awards # 1847632 and # 1750786 (TDTR measurements). In addition, Zhifeng Ren acknowledges support by the Office of Naval Research (ONR) under MURI Award N00014-16-1-2436 (sample synthesis).

Author contributions

R.B.W, C.L., and X.C. originated the research. S.H., C.L., and R.B.W. designed the experiments. S.H. carried out the TDTR experiments with the assistance and supervision of R.B.W and B.S. S.H. prepared the sample for DAC with the assistance and supervision of C.L. and S.W. S.H conducted the TDTR data analysis and simulation with the supervision of R.B.W and C.L. F.T grew the sample with the supervision of Z.R. Q.C. conducted the Raman scattering experiments. Y.X. contributed to single-crystal X-ray diffraction measurements. All authors discussed the results. S.H., C.L., and R.B.W. wrote the manuscript with contributions from all authors.

Competing interests

The authors declare no competing interests.